Asian Journal of Chemistry; Vol. 31, No. 12 (2019), 2865-2870

ASIAN JOURNAL OF CHEMISTRY

https://doi.org/10.14233/ajchem.2019.22256

Influence of Fuel on Structure, Morphology, Magnetic Properties and Photocatalytic Activity of $NiFe_2O_4$ Nanoparticles

LOAN T.T. NGUYEN[1,*], LAN T.H. NGUYEN[1], N.T.T. HANG[2], NGUYEN QUANG HAI[3], VU THI HAU[1], DUY TRINH NGUYEN[4,5] and TO-UYEN T. DAO[4,5]

[1]Faculty of Chemistry, Thai Nguyen University of Education, Thai Nguyen University, Thái Nguyên, Vietnam
[2]Thai Nguyen University of Technology, Thai Nguyen University, Thái Nguyên, Vietnam
[3]Faculty of Physics, Thai Nguyen University of Education, Thai Nguyen University, Thái Nguyên, Vietnam
[4]NTT Hi-Tech Institute, Nguyen Tat Thanh University, Ho Chi Minh City, Vietnam
[5]Center of Excellence for Green Energy and Environmental Nanomaterials, Nguyen Tat Thanh University, Ho Chi Minh City, Vietnam

*Corresponding author: E-mail: nguyentoloan@dhsptn.edu.vn

Received: 5 June 2019; *Accepted*: 30 July 2019; *Published online*: 16 November 2019; AJC-19633

The present study attempted the synthesis of nickel ferrite ($NiFe_2O_4$) nanoparticles *via* solution combustion technique with urea as the fuel. The synthesized samples was structurally characterized by a series of different techniques including TGA/DSC, X-ray powder diffraction, energy dispersive X-ray, scanning electron microscope, transmission electronic microscopy, Brunauer-Emmett-Teller and Fourier transform infrared spectroscopy. A vibrating sample magnetometer (VSM) was also employed to investigate the magnetic properties of nickel ferrite at room temperature. The results showed that the crystallite size of the $NiFe_2O_4$ nanoparticles declined from 45.8 to 33.7 nm in response to elevated amount of urea in the precursor. The photocatalytic activity of $NiFe_2O_4$ nanoparticles was investigated by using rhodamine B dye under visible light.

Keywords: Nickel ferrite, Nanoparticles, Solution combustion method, Urea, Photocatalytic activity, Magnetic properties.

INTRODUCTION

Among magnetic materials, nanocrystalline spinel ferrites are a class of important material that exhibits a wide range of interesting properties including desirable grain size and chemical and thermal stabilities [1]. The materials find numerous applications various fields such as catalysts [2,3], gas sensors [4,5], electronic device, anode materials for lithium ion batteries [6] and microwave devices [7]. One recently discovered application of ferrites with spinel-type structure is as industrial catalysts for removal of dyes [8]. However, the photocatalytic efficiency of the material is determined by various factors including distribution, size and shape of particles and more importantly the selected synthesis method. Such methods to obtain the ferrite with spinel structure may range from the hydrothermal method [9], sol-gel method [10], co-precipitation [2] to combustion method [8,11].

One type of spinel ferrites, $NiFe_2O_4$, is prominent due to its advantages including low coercivity, high electrical resistivity, low eddy current loss and remarkable thermal and chemical stability [4]. Structurally, $NiFe_2O_4$ nanoparticles manifests in inverse spinel cubic structure where the tetrahedral site (A site) and the octahedral site (B site) are populated by Fe^{3+} ions and the combination of Ni^{2+} and Fe^{3+} ions, respectively [12]. To synthesize $NiFe_2O_4$ nanoparticles, the technique of combustion could be employed with the use of glycine [8,13,14], citric acid [12,15], sucrose [14] or urea [11,16] as chelating/fuel agents. The technique is first initiated with the formation of a gel, followed by combustion of a solution consisting of the precursor salts of interest and the reducing agent. Since the combustion method allows a one-step, quick, convenient synthesis process, consumes low external energy and produces crystalline nanoparticles with homogeneous structure, this method is preferred to other synthesis techniques.

The aim of the present study is to investigate the effect of the molar ratio of fuel and oxidation on the structure, morphology, magnetic properties and photocatalytic activity of $NiFe_2O_4$ nanoparticles synthesized by solution combustion.

EXPERIMENTAL

Nickel nitrate hexahydrate [$Ni(NO_3)_2{\cdot}6H_2O$], urea (CH_4N_2O), iron nitrate nonahydrate [$Fe(NO_3)_3{\cdot}9H_2O$] and rhodamine B ($C_{28}H_{31}ClN_2O_3$) were purchased from Merck and used as received.

Preparation of $NiFe_2O_4$ nanoparticles: Three samples of $NiFe_2O_4$ nanoparticles, denoted as NF1, NF2 and NF3, were prepared with molar ratio of urea: $Ni(NO_3)_2{\cdot}6H_2O$: $Fe(NO_3)_3{\cdot}9H_2O$ of (1, 3 and 6):1:2, respectively. First, urea was dissolved in the water. Subsequently, $Ni(NO_3)_2{\cdot}6H_2O$, $Fe(NO_3)_3{\cdot}9H_2O$ was added to the solution under vigorous stirring to form a mixed solution. The amount of added $Ni(NO_3)_2{\cdot}6H_2O$, $Fe(NO_3)_3{\cdot}9H_2O$ corresponds the desired molecular ratio. The mixed solution was further stirred for 4 h to obtain a gel, which was dried in an oven at 70 °C for 12 h to obtain the powder samples. Lastly, calcination of the powder took place at 500 °C for 3 h with a heat rate of 5 °C. min^{-1} to obtain the final product [17].

Characterizations: X-ray diffraction (XRD) with a D8 Advance diffractometer (Brucker, Madison, WI, USA) with CuK_α radiation (λ = 1.5406 Å) in a 2θ angle ranging from 20° to 70° with a step of 0.03° was employed to characterize the phase of the product. Scherrer's formula was used to calculate the crystallite size, D as follows:

$$D = \frac{k\lambda}{\beta\cos\theta} \quad (1)$$

where λ k β and θ is the X-ray wavelength (0.1504 nm), Scherrer's constant (k = 0.89), the full width at half maximum observed in radians and the angle of diffraction of the (311) peak with the highest intensity, respectively.

For morphological characterization the sample, Hitachi S-4800 (Japan) and JEOL-JEM-1010 (Japan) instruments were used to perform scanning electron microscope (SEM) and transmission electron microscopy (TEM), respectively. For determination of composition of the samples, energy dispersive X-ray spectroscopy (EDX, JEOL JED 2300 Analysis Station, Japan) was performed. N_2-sorption experiments was performed to derive the Bet-specific surface area of nickel ferrite powders. A Quantachrome Nova 2200 surface analyzer instrument was used to determine isotherm at 77 K. The Brunauer-Emmet-Teller (BET) method was used to calculate the specific surface area. Affinity-1S (Shimadzu, Japan) instrument was used to perform Fourier transform infrared spectroscopy (FTIR) for verification of the formation of spinel structure. UV-Vis absorption spectrometer (U-4100, Hitachi, Japan) was used to observe optical absorption spectra. Investigation of magnetic properties of nickel ferrite was conducted using a vibrating sample magnetometer (VSM) at room temperature.

Photocatalytic degradation of rhodamine B: Photocatalytic experiments were carried out in a continuous circulation mode at room temperature. The pH of rhodamine B (RhB) solution was maintained at 6. First, the suspension was stirred for 0.5 h in a dark condition to reach adsorption/desorption equilibrium. Following that, 50 mg of $NiFe_2O_4$ was dispersed in 100 mL of aqueous solution of rhodamine B (10 mg L^{-1}). Subsequently, H_2O_2 was added, followed by immediate irradiation using 40 W compact lamps (Philips). UV-1700 Shimadzu (Japan) ultraviolet-visible spectrophotometer was used to determine the concentration of rhodamine B at 553 nm. The photocatalytic efficiency of rhodamine B (H) was calculated by the equation:

$$H(\%) = \frac{C_o - C_t}{C_o} \times 100 \quad (2)$$

where C_o is taken as the equilibrium concentration of rhodamine B (mg L^{-1}) after dark adsorption and C_t is the concentration of rhodamine B after time t irradiation.

RESULTS AND DISCUSSION

Fig. 1 showed the X-ray diffraction spectra of $NiFe_2O_4$ nanoparticles calcined at 500 °C. It was visually indicated that all three ferrite samples exhibited five characteristic peaks at (220), (311), (400), (511) and (440), which are consistent with cubic spinel structure (JCPDS Card. No. 00-054-0964) [14]. With the increasing the amount of urea, the crystallite size of $NiFe_2O_4$ decreases from 45.8 to 33.7 nm, as shown in Table-1. The lattice parameter for the three samples of $NiFe_2O_4$ nanoparticles varies from 8.3247-8.3413 Å.

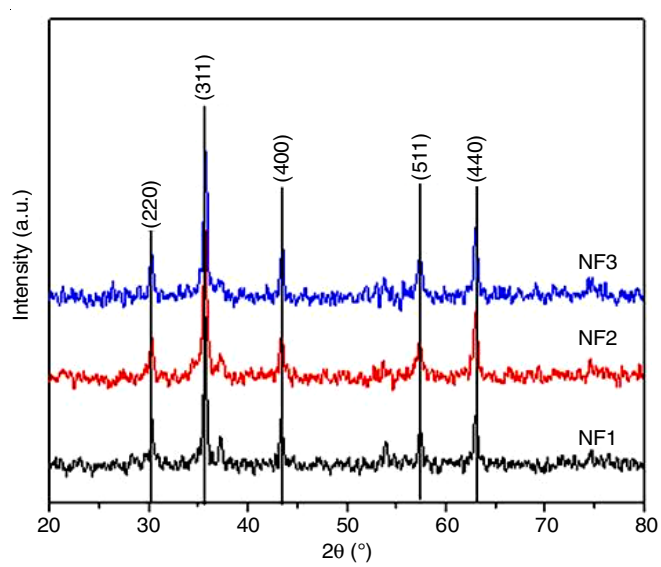

Fig. 1. X-ray diffraction of NF1, NF2 and NF3 samples calcined at 500 °C

TABLE-1
AVERAGE CRYSTALLITE SIZE, LATTICE PARAMETER AND UNIT CELL VOLUME OF THE SAMPLES AT DIFFERENT RATIO MOLE UREA

Samples	Average crystallite size (nm)	Lattice constant (Å)	Cell volume ($Å^3$)
NF1	45.8	8.3347	578.99
NF2	38.6	8.3413	580.36
NF3	33.7	8.3247	576.90

Fig. 2 displayed the FTIR spectra of the $NiFe_2O_4$ samples calcined at 500 °C in the wavelength range from 4000 to 400 cm^{-1}. In all three samples, two broad absorption bands were observed. The first broad band, respectively detected at 3149,

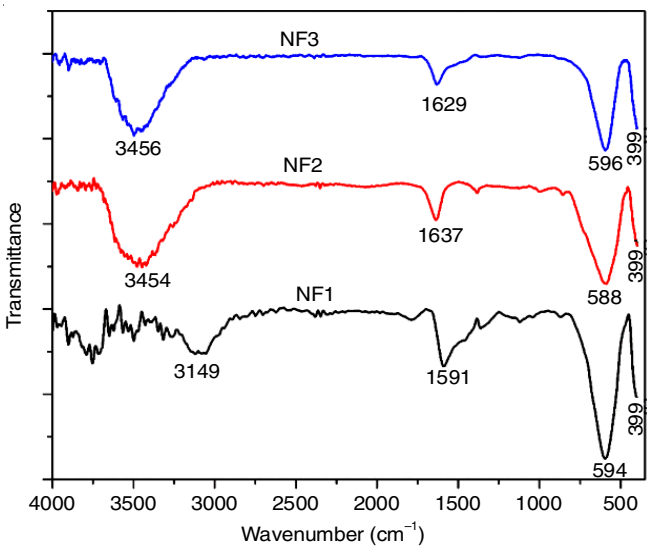

Fig. 2. FT-IR spectra of NF1, NF2 and NF_3 samples calcined at 500 °C

3454 and 3456 cm^{-1} at NF1, NF2 and NF3 sample, could be attributable to the existence of hydroxyl groups (-OH). The second broad band, respectively observed at 1591, 1637 and 1629 cm^{-1} for NF1, NF2 and NF3 sample, could be assigned to the stretching vibration of the carboxyl group [16]. The vibrational band at around 596–588 cm^{-1} and at 399 cm^{-1}, respectively coincides with the intrinsic stretching vibration of metals at tetrahedral sites and octahedral metal stretching [14]. Therefore, it could be concluded that the spinel structured nickel ferrite was successfully formed [17].

The SEM images of $NiFe_2O_4$ samples with different fuel rations (NF1, NF2 and NF3) annealed at 500 °C are shown in Fig. 3(a-c). At first glance, the images were consistent with the foresaid XRD results. To be specific, particle size of the synthesized samples was inversely correlated with the ratio fuel. The NF3 sample was further examined with the TEM images, as presented in Fig. 3(d), indicating the average crystallite size of approximately 25 nm for the NF3 sample.

Fig. 4 showed Energy Dispersive X-ray analysis (EDX) of $NiFe_2O_4$ nanoparticles. It could be observed that samples contained Ni, O and Fe and no impurities, as indicated by the presence of the corresponding peaks without other characteristic peaks.

The size and specific surface area of photocatalysts are important parameters for achieving the efficient photocatalysis. Fig. 5(a) showed the BET plots of nickel ferrite nanoparticles. In addition, Table-2 reported the specific surface area and C constant of the three samples. The specific surface area of NF3 sample is the largest, at 44.94 m^2 g^{-1} while the figure NF1 was 23.24 m^2 g^{-1}, which is the lowest area among the three samples. However, this minimum specific surface area is still larger than

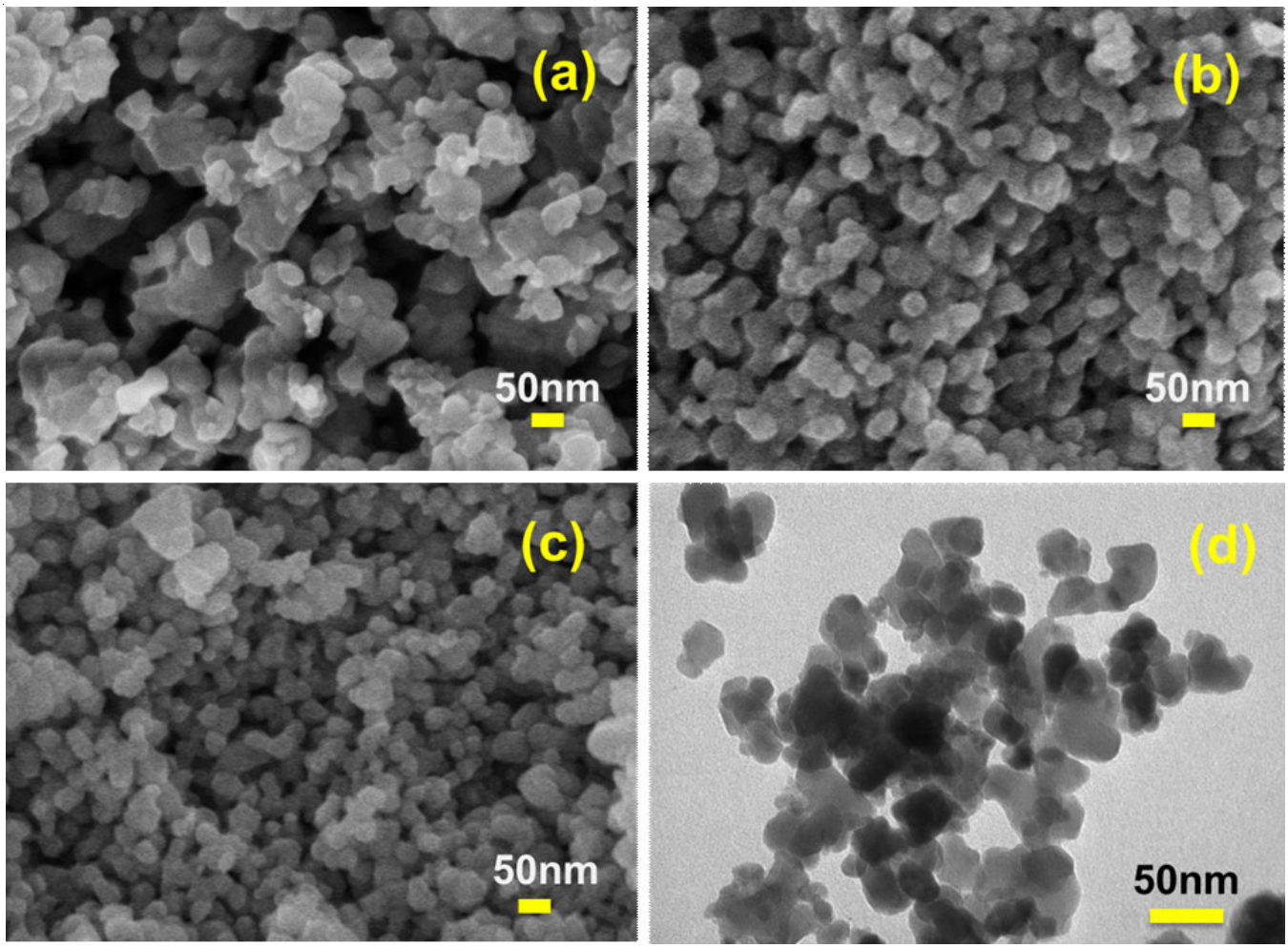

Fig. 3. SEM of $NiFe_2O_4$ nanoparticles: NF1 (a), NF2 (b), NF3 (c) and TEM of NF3 (d)

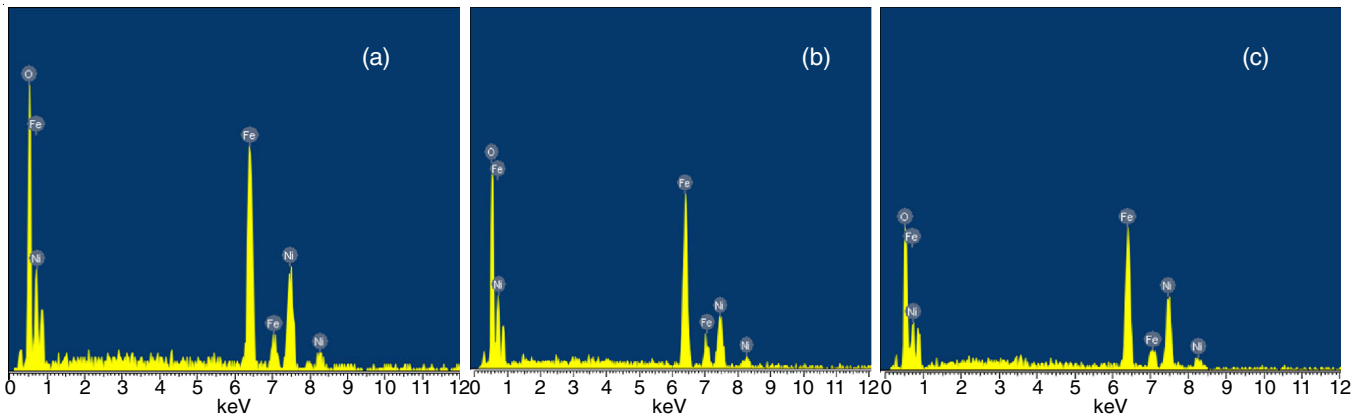

Fig. 4. EDX of $NiFe_2O_4$ particles: NF1(a), NF2 (b) and NF3 (c)

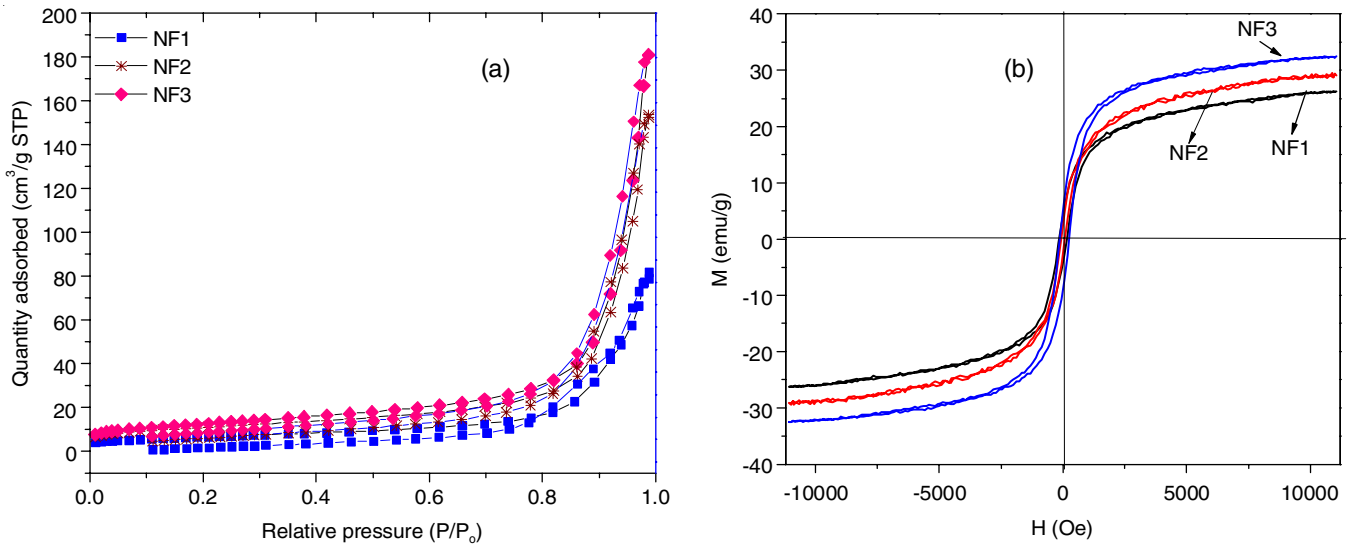

Fig. 5. BET plots (a) and the magnetic loops of $NiFe_2O_4$ nanoparticles (b)

TABLE-2
BET SURFACE AREA AND MAGNETIC PROPERTIES OF $NiFe_2O_4$ NANOPARTICLES

Samples	Surface area (m^2 g^{-1})	C constant	M_s (emu/g)	M_r (emu/g)	H_c (Oe)
NF1	23.24	128.68	26.24	5.17	156.63
NF2	38.88	141.40	29.06	2.85	78.87
NF3	44.94	133.32	32.47	5.51	242.39

that of $NiFe_2O_4$ prepared by the solution combustion using glycine as fuel and other methods [14].

Fig. 5(b) illustrates the magnetic hysteresis loops of the synthesized ferrite samples at room temperature. From the hysteresis curve, some indicators including saturation magnetization (M_s), coercivity (H_c), remanence (M_r) were derived and reported in Table-2. Clearly, the saturation magnetization, M_s was negatively correlated with the fuel ratio. To be specific, the largest saturation magnetization value, at 32.47 emu g^{-1}, was attained in the the NF3 sample while the lowest value at 26.24 emu g^{-1} was found for the NF1 sample. This could be justified by larger grains and improved crystallinity, as evidenced by similar reports for Mn-$CuFe_2O_4$ nanoparticles [18].

Photocatalytic activity of nickel ferrite nanoparticles: Fig. 6(a-c) displays the UV-visible spectra of rhodamine B. in the presence of $NiFe_2O_4$ photocatalyst and H_2O_2 under visible light irradiation. For all samples, the peak intensity at around 553 nm was found to decline gradually by increasing irradiation time. After 270 min of lighting, degradation efficiency of rhodamine B increased from 63.75 % (in presence of NF1) to 94.66 % (in presence of NF3). It is also worth mentioning that NF3 showed the smallest crystal size and highest surface area which may be considered as the main factors responsible for the enhanced photo degradation of rhodamine B.

Dye removal efficiency of the catalyst is assessed through the kinetic study of dye degradation process [19,20]. In this study, Langmuir-Hinshelwood model was employed to describe the photodegradation process as follows:

$$\ln \frac{C_o}{C_t} = kt$$

where C_o and C_t represent the dye initial concentration and the dye concentration at time t (min), respectively. k is the first-order rate constant. Fig. 6d shows the plots of $\ln(C_o/C_t)$ against irradiation time (t) for the $NiFe_2O_4$ samples. High coefficients of determination (R^2) observed in the regressions for three samples indicated that the photodegradation of rhodamine B closely follows a pseudo-first-order reaction, which is similar to results for methylene blue dye in presence $CoFe_2O_4$ nanoparticles [21] or $NiFe_2O_4$ [22]. Further calculations showed

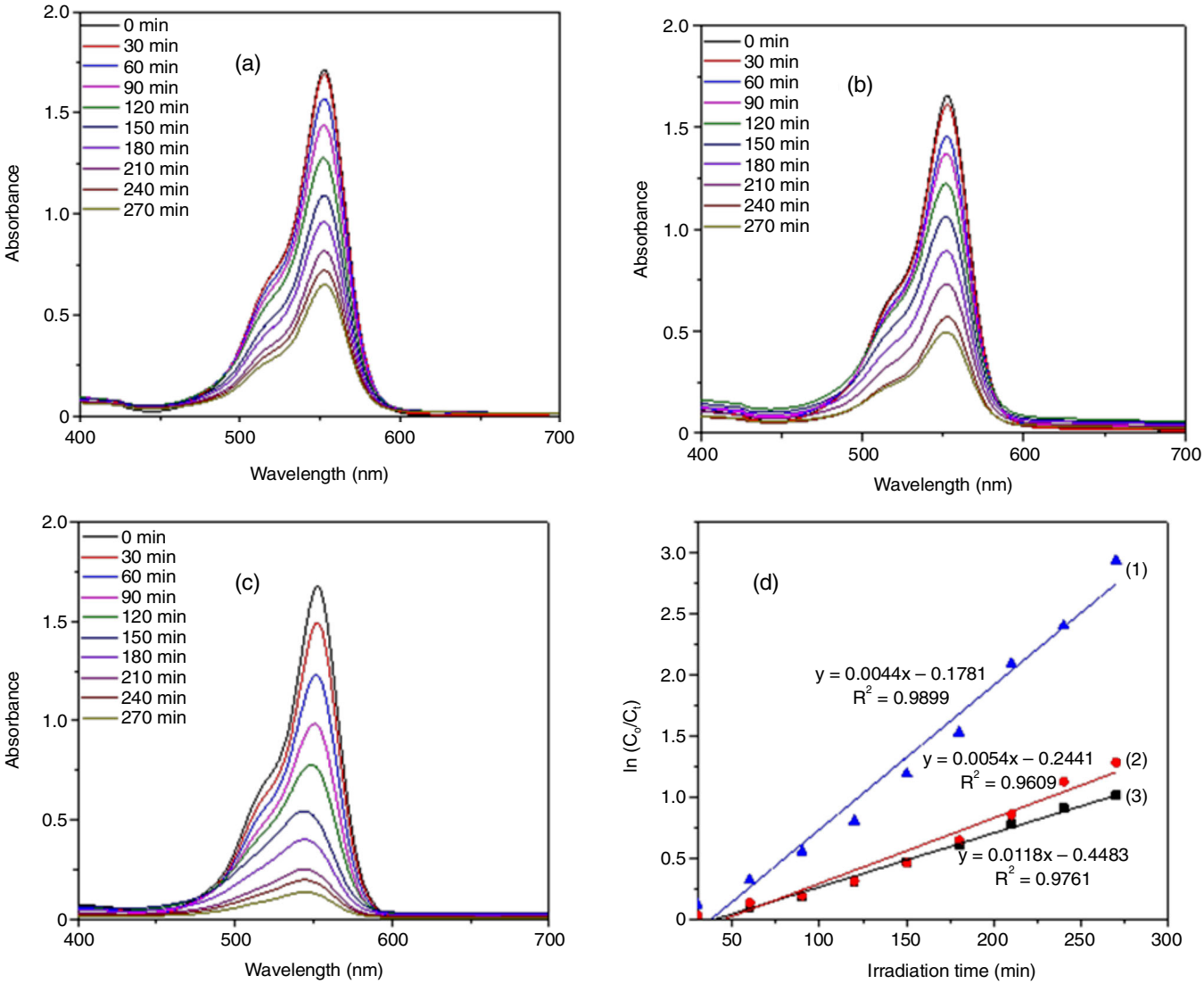

Fig. 6. UV-visible spectra of rhodamine B in the presence of H_2O_2 and $NiFe_2O_4$ nanoparticles: (a) NF1, (b) NF2, (c) NF3 and (d) the plots of $\ln(C_o/C_t)$ *versus* irradiation time (t) in the presence of NF1 (1), NF2 (2) and NF3 (3)

that rate of photodegradation improves with higher dose of urea in the precursor (Table-3). The k_1 for NF3 is 1.18×10^{-2} min^{-1} and is around 2.6 times faster than NF1. This could be explained by enlarged surface area of the NF3 due to the reduction in the particle size, compared with other two samples, which could offer greater active surface and in turn enhanced photocatalytic efficiency [21,23].

TABLE-3
DEGRADATION EFFICIENCY OF RHODAMINE B (H), RATE CONSTANT (k) AND REGRESSION COEFFICIENT (R^2) IN THE PRESENCE OF $NiFe_2O_4$ NANOPARTICLES

Samples	H (%)	k (min^{-1})	R^2
NF1	63.75	0.0044	0.9899
NF2	72.24	0.0054	0.9609
NF3	94.66	0.0118	0.9761

Conclusion

$NiFe_2O_4$ nanoparticles were successfully synthesized by solution combustion method using urea as fuel. Among the synthesized $NiFe_2O_4$ samples, the sample having highest urea ratio possesses the smallest particle size and the highest specific surface area. Under the visible light, degradation efficiency of rhodamine B reached 94.66 % after 270 min. By estimating photo-degradation kinetics, it was found that the photocatalytic reaction of the as-synthesized materials followed the pseudo-first order. Since the synthesized materials could be magnetically recovered and recycled, it is suggested that $NiFe_2O_4$ nanoparticles could act as photocatalysts for applications involving decontamination of organic pollutants in industrially discharged effluents.

CONFLICT OF INTEREST

The authors declare that there is no conflict of interests regarding the publication of this article.

REFERENCES

1. B. Godbole, N. Badera, S.B. Shrivastava, D. Jain, L.S.S. Chandra and V. Ganesan, *Phys. Procedia*, **49**, 58 (2013); https://doi.org/10.1016/j.phpro.2013.10.011.
2. Z. Zhu, X. Li, Q. Zhao, Y. Li, C. Sun and Y. Cao, *Mater. Res. Bull.*, **48**, 2927 (2013); https://doi.org/10.1016/j.materresbull.2013.04.042.

3. A. Sudhaik, P. Raizada, P. Shandilya and P. Singh, *J. Environ. Chem. Eng.*, **6**, 3874 (2018); https://doi.org/10.1016/j.jece.2018.05.039.
4. R.S. Yadav, I. Kuøitka, J. Vilcakova, J. Havlica, J. Masilko, L. Kalina, J. Tkacz, V. Enev and M. Hajdúchová, *J. Phys. Chem. Solids*, **107**, 150 (2017); https://doi.org/10.1016/j.jpcs.2017.04.004.
5. A.F.S. Abu-Hani, S.T. Mahmoud, F. Awwad and A.I. Ayesh, *Sens. Actuators B Chem.*, **241**, 1179 (2017); https://doi.org/10.1016/j.snb.2016.10.016.
6. X. Tang, X. Hou, L. Yao, S. Hu, X. Liu and L. Xiang, *Mater. Res. Bull.*, **57**, 127 (2014); https://doi.org/10.1016/j.materresbull.2014.05.038.
7. S. Joshi, M. Kumar, H. Pandey, M. Singh and P. Pal, *J. Alloys Compd.*, **768**, 287 (2018); https://doi.org/10.1016/j.jallcom.2018.07.250.
8. A.M. Dumitrescu, P.M. Samoila, V. Nica, F. Doroftei, A.R. Iordan and M.N. Palamaru, *Powder Technol.*, **243**, 9 (2013); https://doi.org/10.1016/j.powtec.2013.03.033.
9. T. Peng, X. Zhang, H. Lv and L. Zan, *Catal. Commun.*, **28**, 116 (2012); https://doi.org/10.1016/j.catcom.2012.08.031.
10. M. Srivastava, S. Chaubey and A.K. Ojha, *Mater. Chem. Phys.*, **118**, 174 (2009); https://doi.org/10.1016/j.matchemphys.2009.07.023.
11. E. Ranjith Kumar, R. Jayaprakash and S. Kumar, *Mater. Sci. Semicond. Process.*, **17**, 173 (2014); https://doi.org/10.1016/j.mssp.2013.09.003.
12. A. Ahlawat, V.G. Sathe, V.R. Reddy and A. Gupta, *J. Magn. Magn. Mater.*, **323**, 2049 (2011); https://doi.org/10.1016/j.jmmm.2011.03.017.
13. M. Kooti and A.N. Sedeh, *J. Mater. Sci. Technol.*, **29**, 34 (2013); https://doi.org/10.1016/j.jmst.2012.11.016.
14. T. Lazarova, M. Georgieva, D. Tzankov, D. Voykova, L. Aleksandrov, Z. Cherkezova-Zheleva and D. Kovacheva, *J. Alloys Compd.*, **700**, 272 (2017); https://doi.org/10.1016/j.jallcom.2017.01.055.
15. J. Azadmanjiri, S.A. Seyyed Ebrahimi and H.K. Salehani, *Ceram. Int.*, **33**, 1623 (2007); https://doi.org/10.1016/j.ceramint.2006.05.007.
16. K. Shetty, L. Renuka, H.P. Nagaswarupa, H. Nagabhushana, K.S. Anantharaju, D. Rangappa, S.C. Prashantha and K. Ashwini, *Mater. Today: Proc.*, **4**, 11806 (2017); https://doi.org/10.1016/j.matpr.2017.09.098.
17. J.Y. Patil, D.Y. Nadargi, J.L. Gurav, I.S. Mulla and S.S. Suryavanshi, *Mater. Lett.*, **124**, 144 (2014); https://doi.org/10.1016/j.matlet.2014.03.051.
18. E. Ranjith Kumar, R. Jayaprakash and J. Chandrasekaran, *Superlatt. Microstruct.*, **64**, 343 (2013); https://doi.org/10.1016/j.spmi.2013.10.001.
19. X. Guo, K. Wang, D. Li and J. Qin, *Appl. Surf. Sci.*, **420**, 792 (2017); https://doi.org/10.1016/j.apsusc.2017.05.178.
20. P. Falak, S.A. Hassanzadeh-Tabrizi and A. Saffar-Teluri, *J. Magn. Magn. Mater.*, **441**, 98 (2017); https://doi.org/10.1016/j.jmmm.2017.05.044.
21. A. Kalam, A.G. Al-Sehemi, M. Assiri, G. Du, T. Ahmad, I. Ahmad and M. Pannipara, *Results in Physics*, **8**, 1046 (2018); https://doi.org/10.1016/j.rinp.2018.01.045.
22. P.A. Vinosha, B. Xavier, A. Ashwini, L.A. Mely and S.J. Das, *Optik*, **137**, 244 (2017); https://doi.org/10.1016/j.ijleo.2017.02.089.
23. S.K. Rashmi, H.S.B. Naik, H. Jayadevappa, C.N. Sudhamani, S.B. Patil and M.M. Naik, *J. Solid State Chem.*, **255**, 178 (2017); https://doi.org/10.1016/j.jssc.2017.08.013.